In-situ observation of marine aggregates using imaging devices : turbulence and aggregation

学位名	修士（海洋科学）
学位授与機関	東京海洋大学
学位授与年度	2015
URL	http://id.nii.ac.jp/1342/00001512/

修士学位論文

In-situ observation of marine aggregates using imaging devices: turbulence and aggregation

(光学機器を用いた微小凝集体の現場観測 ―乱流と凝集体の関係)

平成 27 年度

(2016 年 3 月)

東京海洋大学大学院
海洋科学技術研究科
海洋環境保全学専攻

竹内 茉莉香

Chapter 1: Introduction

Flocculated particles consisting of organic and inorganic matter, commonly known as marine snow or marine aggregates have some remarkable impacts on marine ecosystems. For example, increase in particle size by flocculation accelerates their sinking velocity (Laurenceau-Cornex, et al., 2015). Therefore, the contribution of marine aggregates to the biological pump or material transport to the deeper ocean is significantly large (Puskaric, 2012; Flower & Knauer, 1986; Kindler, et al., 2010; Riebesell, 1991). As various materials are trapped in the aggregates, living organisms inside the aggregates can obtain nutrients efficiently even in oligotrophic environment. (Goldman, 1984). Organic matter leaks from the aggregates due to the internal food chain and external predation. The leaked organic matter is an important nutrient supply to the ambient environment, and attracts zooplankton and bacteria (Kiørboe, 2001).

Physical mechanisms, Brownian motion, differential sinking and turbulence promote coagulation of aggregates (McCave, 1975). The collision rate due to turbulence is higher than that of Brownian motion and differential sinking. Turbulence is also known to control the disaggregation process (Colomer, et al., 2005; McCave, 1984; Serra, et al., 2008). Therefore the better understanding of the role of turbulence in the aggregation and disaggregation processes is vital for the predictions of the marine ecosystems. However, *in-situ* observations of aggregates by physical contact such as bottle sampling or net sampling are challenging. This is because transparent exopolymer particles (TEP) secreted by phytoplankton hold the materials together to form aggregates, but also make them extremely fragile (Chow, et al., 2015; Alldredge, et al., 1993; Bar-Zeev, et al., 2012). Some studies used scuba divers to collect aggregates without destroying them, however, the number of aggregates they could collect was limited (Puskaric, 2012; Alldredge & Gotschalk, 1988). Accordingly, most of the past studies were based on either theoretical or experimental investigations at the laboratories, and there has been no *in-situ* observational evidence that successfully elucidates the aggregation and disaggregation processes.

Doubell, et al. (2009) conducted an aggregate observation utilising a Digital Still Logger camera (hereinafter DSL camera) mounted on a microstructure profiler TurboMAP-L that carries a high resolution laser fluorescence probe. The laser fluorescence probe resolves 2mm scale fluorescence. The DSL camera recorded large particles in regions where the laser fluorescence probe detected locally high signals, therefore Doubell et al., (2009) hypothesized that the laser fluorescence probe re-

solved marine aggregates and the DSL camera collected the images of these marine aggregates. Despite this, they did not reach a strong conclusion to prove that those particles were marine aggregates as DSL camera cannot resolve the detailed features of aggregates.

A recent technology introduced inline digital holographic systems for marine plankton observations. LISST-HOLO product (Sequoia Scientific, Inc .) is a commercially available holographic system. The system resolves particles $\geq 25\mu m$ which enables us to identify aggregates.

Objectives of the studies in this thesis are (1) to investigate the roles of turbulence in aggregation and disaggregation processes, using *in-situ* data that are collected by a microstructure profiler TurboMAP-L and DSL camera, and (2) to identify detailed structures of aggregates using the inline digital holographic systems. The study of turbulence and aggregation are presented in Chapter2. The potential use of the inline holographic systems in aggregate measurement is examined as well as the detailed structures of aggregates in Chapter3.

Chapter2: In-situ observation of marine aggregates and turbulence using a digital still logger camera

Abstract

Flocculated suspended particles consisting of organic and inorganic matter called marine aggregates or marine snow widely exist in marine environments. Although numerous experiments aiming to explain their coagulation and disaggregation processes due to turbulence have been conducted in previous studies (Serra, et al., 2008; Colomer, et al., 2005), no *in-situ* observation has successfully explained these processes. In this study, in-situ observation data were collected from various marine environments, such as semiclosed bays in subtropical and subarctic regions, oligotrophic western boundary current, and a large monotonic lake, to clarify the relationship between turbulence and aggregation processes.

Doubell et al.,(2009) showed that a Digital Still Logger camera (DSL camera) recorded large suspended particles in the region where locally high fluorescence signals were observed. They hypothesized that the large particles observed by DSL camera were marine aggregates and that the laser fluorescence probe resolved these aggregates. To test their hypothesis we conducted several independent observations using TML and DSL cameras over a 5 year period at 10 different fields; twice in the Kuroshio Current, twice in Tokyo bay, Tateyama bay, Lake Biwa, Otsuchi bay, Oshima island, Miyake island and Jogashima. Locally high fluorescence signals and total volume concentrations of particles ≥ 120μm showed strong correlation. The rate of turbulence kinetic energy dissipation, ε, and aggregates major axis length also showed strong positive correlation, R=0.72. Aspect ratio(minor axis length/major axis length) showed negative correlation with ε, -0.65. Turbulence was shown to be controlling aggregation rate and had a significant influence on the shape of aggregates.

1. Introduction

Flocculated particles consisting of organic and inorganic matter known as aggregates or marine snow are widely seen in the marine environment. Buesseler & Boyd, (2009) estimated that up to 10 billion tons of carbon was annually removed from the epipelagic ocean by general biological pumps and aggregates are known as major biological pump components (Turner, 2015). Shanks, (2002) suggested

that the contribution of marine aggregates to vertical flux of particulate matter to depth were greater than 90% of total.

Furthermore, the aggregates provide efficient nutrient source for organisms inside (Goldman, 1984), which leads to high abundance of phytoplankton within the aggregates and contributes to primary production (Knauer, et al., 1982; Gotschalk & Alldredge, 1989; Alldredge & Gotschalk, 1988). Both internal food chain and external predation can destroy aggregates and supply nutrients to the ambient water (Kiørboe, 2001).

Turbulence is known to promote the coagulation of aggregates (McCave, 1975) and also to control the disaggregation process (Colomer, et al., 2005; McCave, 1984; Serra, et al., 2008). Because particle sinking speed depends on the size (Gregory, 1961), the better clarification of impacts of turbulence on the aggregation and disaggregation processes is necessary to fully understand the functionalities of marine biological pump, which drives marine ecosystems and biogeochemistry. However, *in-situ* observations of aggregates by physical contact such as bottle sampling or net sampling are challenging. This is because Transparent Exopolymer Particles (TEP) that hold particles together to form aggregates make aggregates extremely fragile (Chow, et al., 2015; Alldredge, et al., 1993; Bar-Zeev, et al., 2012; Passow & Alldredge, 1995; Logan, et al., 1995) .Therefore, many past studies examined the influences of turbulence on aggregates by either laboratory experiments or theoretical investigations (Colomer, et al., 2005; Serra, et al., 2008). So far there has been no successful *in-situ* aggregate measurement to explain the impacts of turbulence on aggregates.

In Chapter2, I show numerous simultaneous measurements of aggregates and physical parameters to explain the influences of turbulence on aggregation and disaggregation processes using *in-situ* observation data.

2. Methods

2.1Obs details

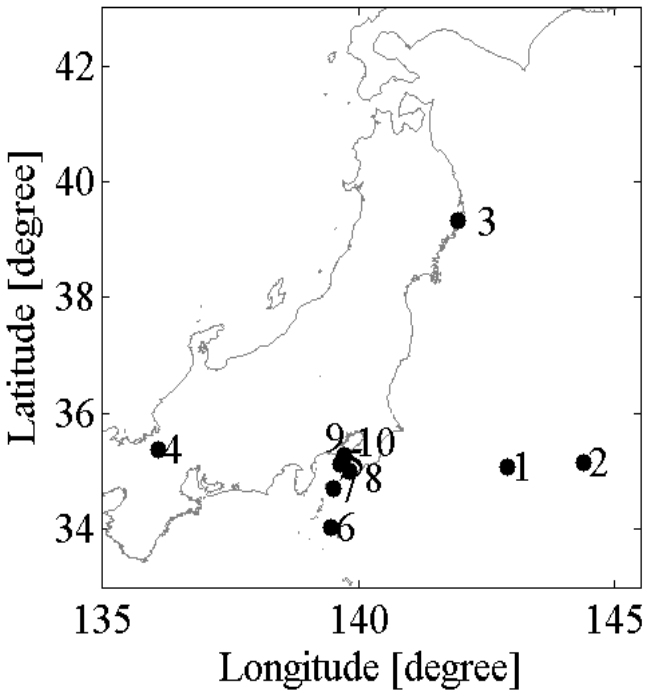

Figure 1-1 Observation fields
1: Kuroshio 09 2: Kuroshio 13 3: Otsuchi 4: Biwa 5:Joga 6:Miyake 7:Oshima 8:Tateyama 9: Tokyo bay Feb 10: Tokyo bay Sep

Table1-1 Observation details

Obs. field	Region	Depth [m]	Latitude [°]	Longitude [°]	Year	Month	Number of images
Kuroshio 09	Open water	1340	35.0683	142.9093	2009	10	21772
Kuroshio 13	Open water	1237	35.159	144.3985	2013	7	4187
Oshima	Open water	663	34.6993	139.5003	2013	6	2289
Miyake	Open water	1274	34.0376	139.4661	2012	6	13238
Tokyo bay	Coast	67	35.272	139.726	2008	2	4860
Joga	Coast	531	35.1243	139.6433	2011	6	5944
Tokyo bay	Coast	67	35.2761	139.7206	2012	9	18455
Otsuchi bay	Coast	28	39.3411	141.9257	2013	9	4187
Tateyama bay	Coast	29	35.0065	139.8296	2014	5	2491
Biwa	Lake	8	35.385	136.0966	2010	8	8466

A series of campaigns was conducted from 2008 to 2013 at 10 different regions that cover coastal regions, open water and a lake in Japan (Table1-1, Figure1-1). Most observations were conducted during summer months, May to October. One observation was performed in the middle of winter at Tokyo bay in 2008. As is shown in Figure1-1, all coastal observation sites are on the Pacific Ocean side of Japan, and open water regions are either close to or in the Kuroshio. Lake Biwa is the largest lake in Japan located on the western side of Japan.

In order to measure aggregates, physical parameters and biological parameters simultaneously, a Digital Still Logger camera (DSL) was mounted on a microstructure profiler, TurboMAP-L. The DSL camera used the LED fluorescence probe as

a light source. As the light source is weak, measurements were conducted only during night time to prevent sunlight disturbance.

2.2 Instruments

2.2.1 Turbulence Ocean Microstructure Acquisition Profiler – Laser (TurboMAP-L)

Figure 1-2 TurboMAP-L
a: TurboMAP-L
b: TurboMAP-L deployment in free fall mode.
Recovery is controlled by the winch.

For biological and physical parameter measurements, we utilised the microstructure profiler, TurboMAP-L (TML) which carries a pressure sensor, laser and LED fluorescence sensors, turbidity sensor, conductivity sensor, high accuracy temperature probe and high resolution temperature probe, and two shear probes (Table1-2 and Figure1-2) (Doubell, et al., 2009). The profiler utilises on board power and data for each parameter is collected at 64 – 512 Hz. Collected data is transmitted to a connected computer on the vessel through the cable. During the profiling, the TurboMAP-L is in quasi free fall mode which does not disturb sampling objects or ambient conditions by the instrument. The most significant feature of this instrument is that it carries two fluorescence probes, LED and laser, which are different in their spatial resolution and sampling volume. The LED fluorescence probe is

able to measure a larger sampling volume at 2cm scale resolution whereas the laser fluorescence probe resolves 2mm scale fluorescence in a smaller sampling volume. Doubell, et al., (2009) showed that the laser fluorescence probe detected locally high signals, although 1 metre scale averaged data of laser fluorescence and LED fluorescence showed no difference between the two probes. Doubell et al.,(2009) hypothesized that the locally high laser fluorescence signals are resolved marine aggregates.

Table 1-2 TML specification

Parameters	Range	Accuracy	Resolution	Sampling rate [Hz]
Shear[s^{-1}]	0 to 4	5%	0.0001	512
Fast temperature[degC]	-5 to 45	±0.01	<0.0001	512
Slow temperature[degC]	-5 to 45	± 0.05	0.001	64
Conductivity[mS^{-1}]	0 to 70	± 0.01	0.002	64
Pressure [m]	0 to 500	0.2%	0.01	64
Accelerometers[G]				
X				256
Y	±1	1%	0.0005	256
Z				64
Fluorescence				
LED [ugL^{-1}]	0 to 100	±0.5	0.005	256
Laser				256
Turbidity[ppm]	0 to 100	±1	0.0005	256

2.2.2 Digital Still Logger camera (DSLcamera)

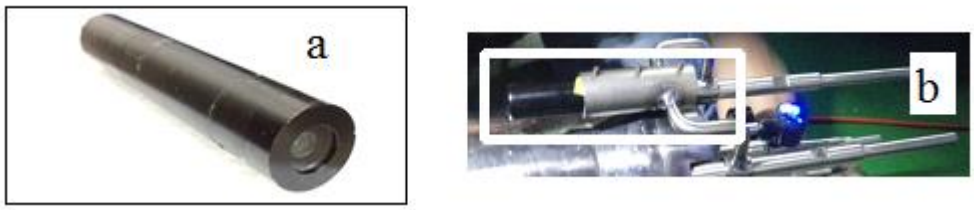

Figure 1-3 Digital Still Logger camera
a : A Digital Still Logger Camera
b : DSL camera mounted on TML using an aluminium frame, facing the direction of travel. LED fluorescence probe is used for light source. As the light source is weak, the observations were conducted only during night time.

Table1-3 DSL specification

Field view [pixels]		Field view [cm]	Cropped image [cm]		Resolution [μm]	Aggregate resolution [μm]	Sampling rate [Hz]
x	1024	6	x	2	59	120	5
y	1280	7.5	y	2			

The Digital Still Logger camera system (DSL camera; DSL 190-VDT2, Little Leonardo Co.) was originally developed for marine mammal research purposes. DSL camera is 2.2cm in diameter, 11.9cm in body length. Its field view is 6×7.5 cm with 59μm per pixel (Table1-3, Fig.1-3). Although the DSL camera carries temperature and pressure sensors, TML depth data was used in order to more accurately measure the depth.

DSL camera was mounted on TML using a special aluminium frame to collect images in the direction of its travel. The LED light from the fluorescence probe was used as the DSL camera light source. The LED probe utilises 6 LEDs that intersect 15 mm away from the surface of the probe. Focal depth of DSL is 10 cm and DSL was mounted on the TML to capture this LED intersection in its focus. As the LED light source was weak, the observations were performed only during night time to prevent light disturbance from sunlight. Sampling speed was 5Hz, collecting 1 frame every 10 cm. All the pictures were compressed and recorded in the internal memory, data transmission was performed manually each time the DSL camera was recovered.

2.3 DATA analysis

Near surface water could be disturbed by research vessels and surface waves . This prevented TML from measuring near surface microstructure accurately. In these near surface layers, bubbles caused by surface wave breaking appeared in the images recorded by the DSL camera. Therefore, the surface data, 0 – 10 metres, were ignored in this study.

To compare the background physical and biological parameters, data were averaged for every 10 metres. Non- averaged data was used for spectrum analysis.

2.3.1 TML analysis – the rate of turbulent kinetic energy dissipation

The rate of turbulence kinetic energy dissipation, ε, was estimated from the shear data, assuming isotropic turbulence (Eq.1-1). The minimum eddy scales, the Kol-

mogorov length scale ($\lambda\varepsilon$), was also calculated by equation1-2, where ν is kinematic viscosity coefficient, u' is horizontal velocity, z is vertical coordinate.

$$\varepsilon = \frac{15}{2}\nu\left(\frac{\partial u\prime}{\partial z}\right)^2 \quad \text{Eq.}\,(1-1)$$

$$\lambda_\varepsilon = \left(\frac{\nu^3}{\varepsilon}\right)^{\frac{1}{4}} \quad \text{Eq.}\,(1-2)$$

In this study, ε was estimated by integrating power spectrum over 2 seconds data segment. In order to avoid integration of the mechanical noise as well as electric noise, spectrum were integrated over the wavenumber range where Nasmyth empirical spectra matched with that from the measurements. The lost shear variance in these noise wavenumber ranges, was recovered by integrating Nasmyth spectra. (Nasmyth, 1970; Oakey & Elliot, 1982).

2.3.2 Integrated laser fluorescence intensity

Doubell, et al., (2009) showed locally high fluorescence signals by the laser fluorescence probe. Such high signals were observed in all the campaigns we conducted. Although they hypothesized that the laser fluorescence probe resolved aggregates by visually comparing the laser fluorescence data to the images collected by DSL camera, more quantitative evidence is required to test this hypothesis. In this study, the laser fluorescence peaks, which are presumably phytoplankton aggregates, are quantitatively extracted by setting a threshold fluorescence at twice the 1 metre moving average. Those signals that exceeded the threshold were integrated for every 10 metres (Eq.1-3 and Fig.1-4). Although different thresholds were tested, 1.5 and 3 times as large as the moving average values, twice the moving average demonstrated the best separation of the locally high signals.

$$\int_{H_i}^{H_i+10} (f(z) - threshold)\, dz \quad \text{Eq.}\,(1-3)$$

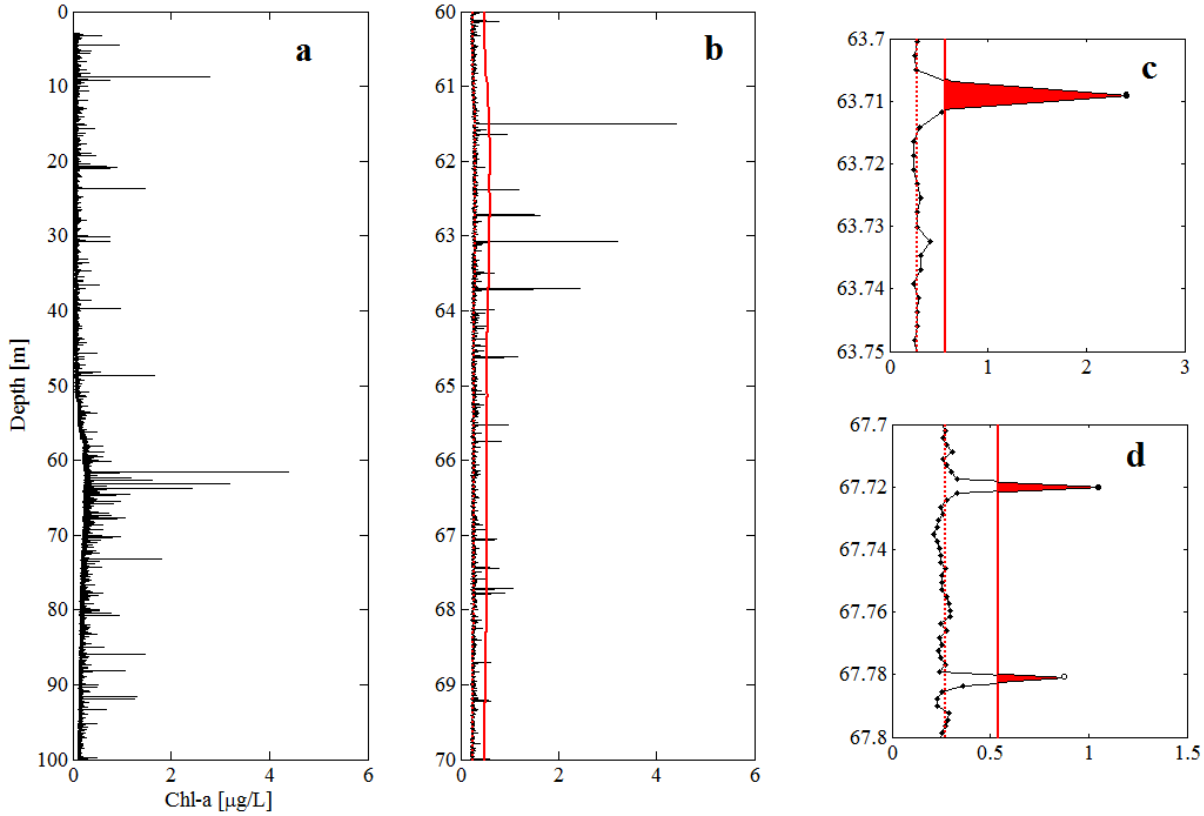

Figure 1-4 Integrated laser fluorescence intensity
a: An example of profile that laser fluorescence probe collected
b: Red line is the threshold. Two times moving average
c and d: Signals exceeded the threshold. The red areas were integrated for every 10 metres.

2.3.3 DSL image process

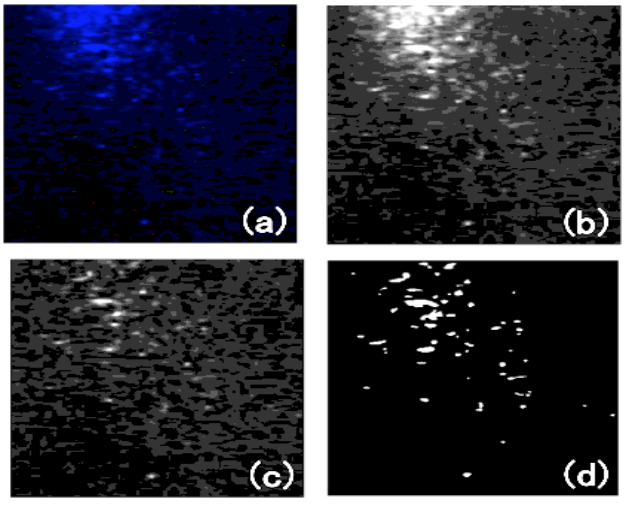

Figure 1-5 DSL image processing
a: Raw image trimmed into 2cm×2cm
b: Blue colour extraction
c: Normalise illumination unbalance
d: Generate binary image

As described in Doubell et al.,(2009), the following operations were processed to use DSL images for the aggregates studies. Firstly images were cropped to 340 × 340 pixels where LED light is projected most strongly. After this cropping only blue colour band was extracted (Fig.1-5 a and b). Unequal distance from the light source over the image field creates non-uniform illumination across the image. To normalise the imbalance of illumination, the intensity of each image was divide by background image intensity. The background image was generated by the average of all images in each deployment after applying a 15 × 15 pixel filter (Fig1-5 c). Threshold was defined by discriminative analysis method and binary images were generated using the threshold (Fig.1-5 d). Individual particle properties such as major and minor axis length, equivalent spherical diameter and area were determined by MATLAB *regionprops* function (The Mathworks Inc., Natick, MA, USA). Volume was estimated from equivalent spherical diameter To separate aggregates and individual plankton cells, only particles having a 5 or more pixel area were defined as aggregates making aggregate resolution > 120 μm. Following the methods described in Doubell, et al., (2009), Franks & Jaffe (2001), Franks & Jaffe(2008), all the particles were screened whether they were in focus. Finally, any unclear images were ignored by visual inspection.

2.3.4Spectrum analysis

The number of particles in each bin class was counted to determine size spectrums. Lognormally increasing bin classes (d) were computed by equation4. The normalised number of particles (n) was computed by counting the number of particles with major axis length (MAL) in each bin class, then dividing them by Δd. The number of particles was plotted against d to express the size spectrum.

$$d = 10^{(2+0.065\times i)}, i=1 \text{ to } 28, \qquad \text{Eq.(1-4)}$$

Particles < 300 μm were ignored as mechanical noise in regression lines fittings. Two regression lines were fitted to each size spectrum.26 cases were tested to find the best fit. First slope (Slope1) was fitted to 1st to j-th bins spectrum, and second slope (Slope2) was fitted to j-th to end, where j=2 to 27. Nf is the theoretical value computed by fitting. Rss was calculated for each case (Eq.5). The fit that had the least Rss was defined as the best fit.

$$R_{ss} = \sum_{1}^{k} (N_k - Nf_k)^2 \quad k=1 \text{to } 28 \qquad \text{Eq.(1-5)}$$

2.3.5 nVd spectrum

Normalised volumetric spectrum (nVd) was computed for volumetric spectrum using the methods described in Petrik, et al., (2013). The volume concentrations were estimated by multiplying n by V, where $V = (\pi/6)d^3$ and n is the size spetrum. Therefore, nV is the volume concentrations in each bin class. Plotting volume concentrations in each bin against particle size, d, does not represent the correct distribution visually, as the bin size in logarithmic graph shrinks the small particle distributions and stretches the large particle distributions. Thus d is multiplied to the volume concentrations to normalise the distributions. The area under the curves of these normalised volume concentrations (nVd) against d represents total volume concentrations. Previous studies reported that volume size spectrums of chained diatoms and aggregate formation from algae had lognormal shape distribution (Kranck & Milligan, 1988; Jackson, 1995). Aggregates distribute log-normally according to Kolmogorov's breakage process (Kolmogorov,1941). Thus Petrick et al., (2011) hypothesized that aggregates distribute lognormally in volumetric spectrum and applied lognormal fitting to separate aggregates and noise, such as nonpassive motile organisms zooplankton, in volumetric spectrums using equation 6

$$\mathrm{nVd_{fit}} = Vagg \frac{1}{\sigma\sqrt{2\pi}} \exp\left(-\frac{(d-\mu)^2}{2\sigma^2}\right) \qquad \text{Eq.}\,(1-6)$$

where μ and σ are peak(log-mean) and width(log standard deviation) of distribution . Vagg is the total volume concentration which is area under the curve of nVd spectrums. We applied this normal fitting to the nVd spectrum to investigate whether obtained particle images by DSL are aggregates.

3. Results

3.1 Characteristics of particles

The laser fluorescence probe detected locally high signals (Fig.1-6). Aggregate particle abundance increased in thermocline where chlorophyll maxima appeared . Integrated laser fluorescence intensity (ILFI) clearly indicated the depth where those locally high signals frequently appeared (Fig.1-6). In order to examine the compositions of particulate matter that DSL camera collected, total volume concentrations of aggregates Vagg were compared to turbidity and ILFI based on the TurboMAP-L measurements. Turbidity and Vagg were averaged for every 10 metres. Comparison between turbidity measured by TurboMAP-L and Vagg from DSL camera showed that DSL successfully collected images of suspended particles. Strong correlation with a correlation coefficient R=0.94 was observed (Fig. 1-7a).

ILFI vs Vagg showed clearly that there are two separate clusters for Vagg within open water (Kuroshio 2009 and 2013, Miyake island and Oshima island) and coastal water (Otsuchi bay, Tokyo bay February and September, Tateyama bay), but with similar values of ILFI (Fig. 71-a). Lake Biwa ILFI and Vagg appeared in the cluster of coastal water (Fig. 1-7a). Open water showed large ILFI despite small Vagg. This implies that numerous phytoplankton are dense in small volume. The correlation coefficient was relatively large for both open water and coastal regions, 0.55 and 0.67, respectively. The strong correlation between turbidity and Vagg, and the moderate correlations found between turbidity and ILFI for both coastal and open waters suggest that the particles identified in the DSL images are suspended particles consisting of high proportions of phytoplankton.

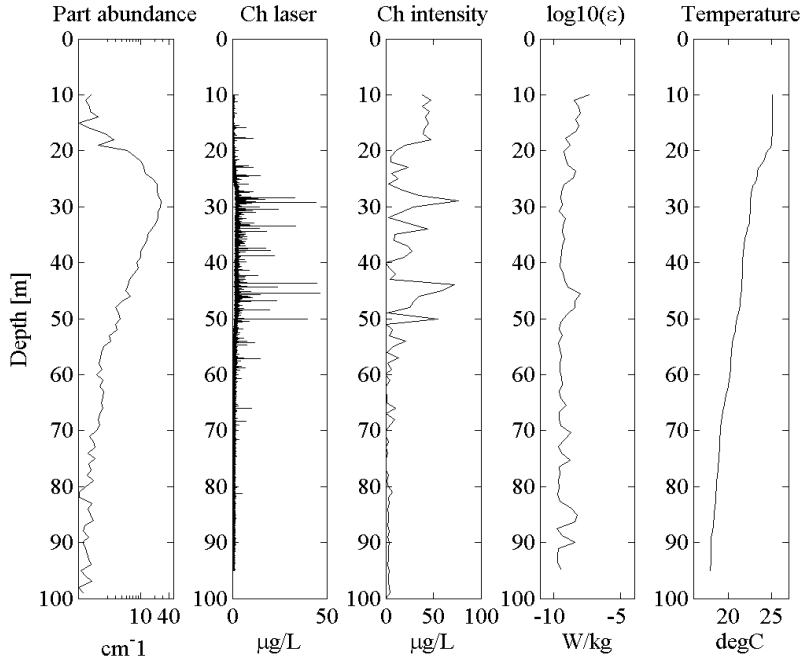

Figure 1- 4 Vertical profile
Kuroshio 13
Particle abundance increased between 20 and 60 metres depth. Laser fluorescence showed locally strong intermittent signals. Integrated laser florescence intensity(ILFI) clearly showed these signals.

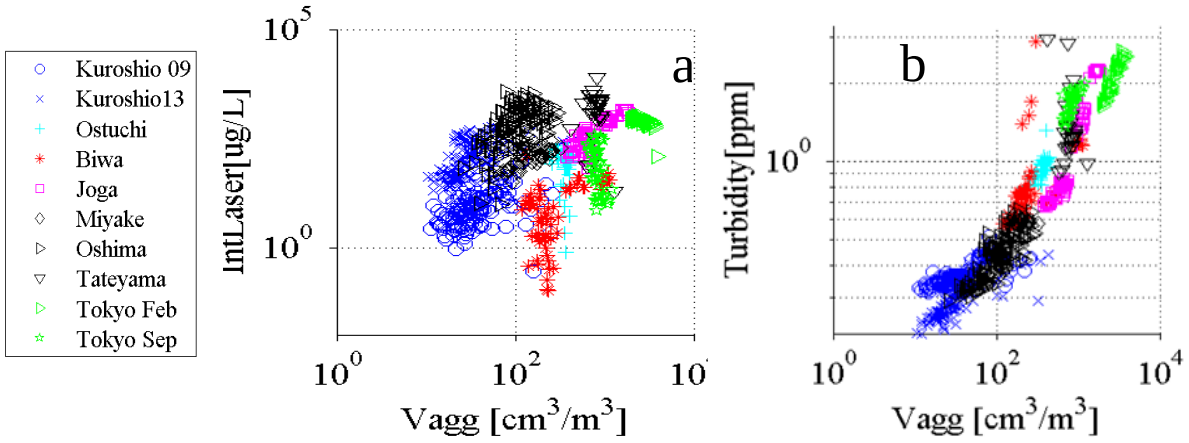

Figure 1-5 Aggregate volume VS IFLI and turbidity
a: IFLI vs aggregate volume concentration. R-total is 0.40, R-coast is 0.67 and R-open water is 0.55.
b: Turbidity vs aggregate volume concentration. R-total is 0.94,R-coast is 0.83 and R-open water is 0.82

The normalised volumetric spectrums, nVd spectrums, were used to verify that those identified particles were aggregates. nVd spectrums showed lognormal distributions (Fig.1-8). According to Kolmogorov's breakage process (Kostoglou, et al., 1997; Podgorska, 2006), objects that can be broken into smaller segments lognormally distribute. Two sample Kolmogorov-Smirnov test was applied to confirm that nVd spectra and lognormal fittings were statistically from the same population. The maximum absolute differences between cumulative distributions of nVd and the lognormal fittings were computed (Table1-4). The critical value Dα was given by $\frac{1.36}{\sqrt{Sample\ number}}$ (Massey, 1951). $D_{0.05}$= 0.31 where α =0.05 (95% confidence interval) and sample number =28. All the D values were smaller than $D_{0.05}$, thus the KS test accepted the null hypothesis that the two distributions were statistically identical. However, the same null hypothesis of the KS was test rejected for fittings of open water dataset with $D_{0.01}$= 0.26. These results suggest that most of the objects that DSL camera recorded were aggregates.

Table 1-4 Kolmogorov-Smirnov test

α	Dα	Kuro-shio09	Kuro-shio13	Otsuchi	Lake Biwa	Joga	Miyake	Oshima	Tateya-ma	Tokyo Feb	Tokyo Sep
		0.30	0.29	0.29	0.29	0.24	0.28	0.21	0.23	0.24	0.23
1%	0.26	-	-	-	-	✔	-	✔	✔	✔	✔
5%	0.31	✔	✔	✔	✔	✔	✔	✔	✔	✔	✔

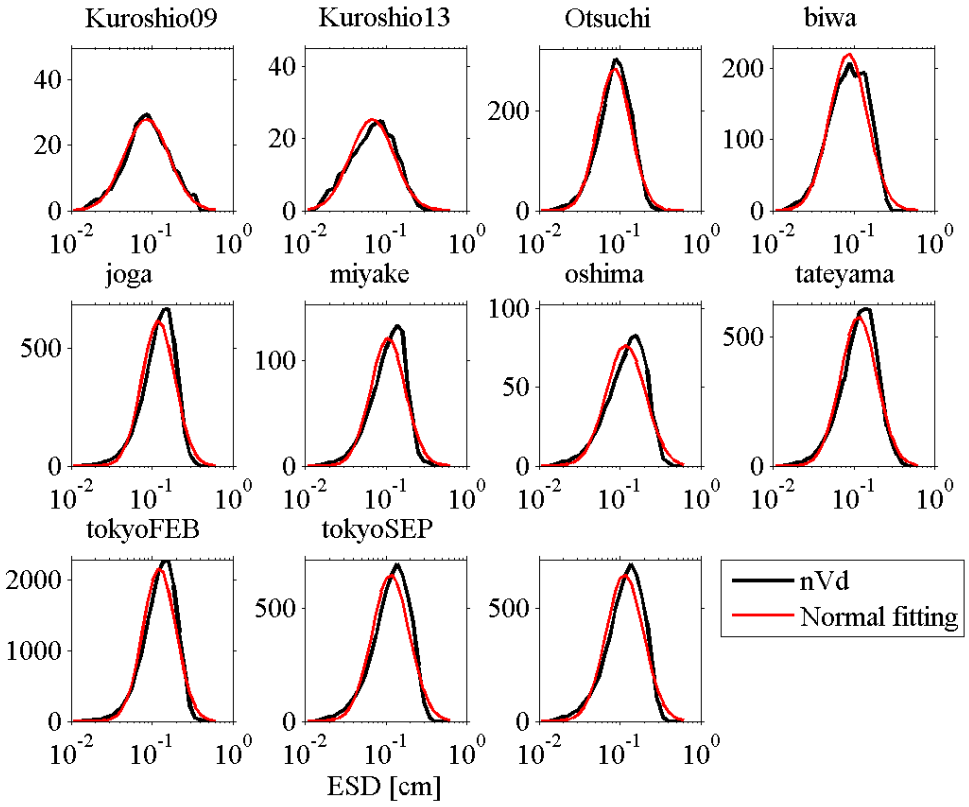

Figure 1-8 nVd fitting
T-test to nVd spectrums and log- normal fittings rejected hypothesis that two distributions are inconsistent. With 0.95 probabilities, they describe the same distributions. Since aggregates have log-normal distributions (Kolmogov's breakage process), particles recorded by DSL are aggregates.

3.2 The size of aggregates and turbulence intensity

In order to investigate the influences of turbulence on aggregation, turbulent kinetic energy dissipation rate ε and MAL were compared. Each data set was averaged for 10 metres (Figure 1-9a). The red line indicates the Kolmogorov scale computed by equation 2. Strong correlation between mean MAL and mean ε was observed; correlation coefficient R=0.72 with p-value <<0.01. 1 metre average and 5 metre average data sets also showed high correlation between MAL and ε ;R_{1m}=0.66, R_{5m}=0.67.Although strong correlation was found over the entire data set, individual fields showed relatively weak correlation; R ranging from -0.15 to 0.66. Individual observations were not able to demonstrate the relationship between turbulence intensity and MAL, whereas combining all data sets showed that aggregates increase in size as turbulence becomes stronger. The long term observations to gather a large number of data sets enabled this study to explain this mechanism.
A limited number of particles exceeded the Kolmogorov scale. This suggests that the Kolmogorov scale is the critical size to determine the maximum size of aggre-

gates. Moreover, there were not many particles exceeded 1mm which is the Kolmogorov scale when $\varepsilon = 10^{-6}$ Wkg^{-1}. In general, only the surface layer and tidal channel indicate strong turbulence with $\varepsilon \approx 10^{-3}$ to 10^{-2} Wkg^{-1}. The ε in most parts of the water column remains smaller than 10^{-6} Wkg^{-1} (Lueck, 2005; McCave, 1984; Kantha & Clayson, 2000). The correlation between ε and MAL within Kolmogorov scale suggests that the aggregation process due to turbulence could be ubiquitous in majority of world's ocean. Once the turbulence reaches its maximum strength in controlling aggregation, $\varepsilon = 10^{-6}$ Wkg^{-1}, the disaggregation process is hypothesized to erode fragile aggregates. A slightly negative correlation, R=-0.19 was found for the data with $\varepsilon > 10^{-6}$ Wkg^{-1}. However, the number of samples was not sufficient to pass the null hypothesis of no correlation with 95% confidence.

3.3 The shape of aggregates and turbulence intensity

The aspect ratio (AR = $\frac{Minor\ axis\ length}{Major\ axis\ length}$) of particles indicates particles' shapes; AR ≈ 0 represents cylindrical shape and AR ≈1 represents spherical shape. Most particles show AR less than 0.5. Thus observed particles were mostly cylindrical in shape, consistent with Riebesell, (1991) (Fig. 1-9b). Decreasing AR as ε increased implied particles tend to be stretched with stronger turbulence. The correlation coefficient R_{10m} was -0.65. The data averaged with smaller bins similarly showed negative correlation coefficient, R_{1m} =-0.53 and R_{5m} = -0.62.

Section 3.2 showed that larger aggregates are formed as turbulence becomes stronger. AR indicated that turbulence is not only promoting the growth of aggregates, they are stretching the aggregates with strong turbulence. Therefore, as the intensity of turbulence increases larger, stretched aggregates are formed.

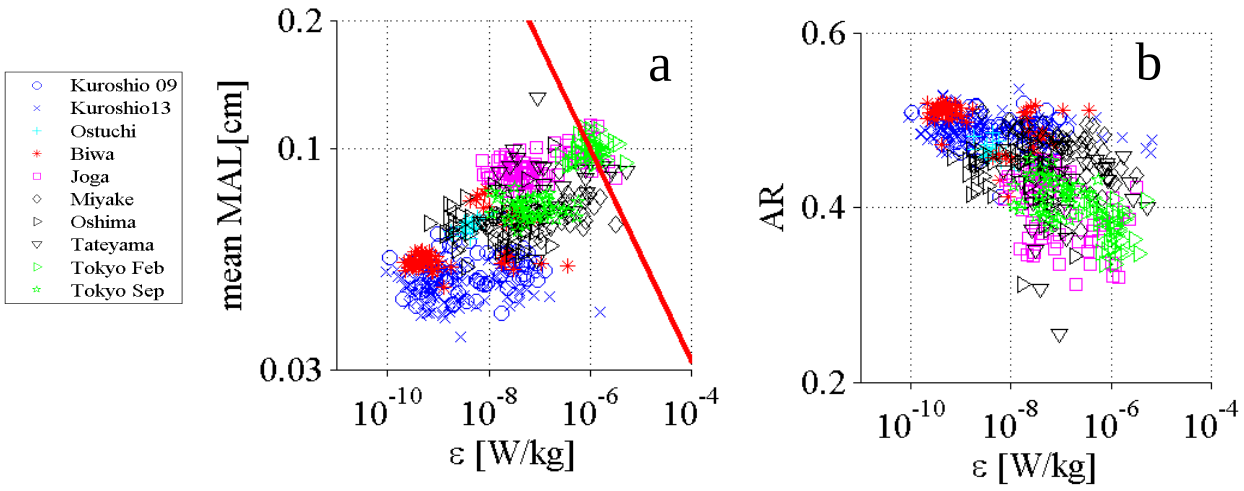

Figure 1-9 ε VS particle properties
a: ε (x-axis) vs mean MAL(y-axis). R-total is 0.72. mean MAL increases with ε. $\varepsilon=10^{-6}$ is a critical value to determine aggregation and disaggregation process.
b: ε vs AR(minor axis length/ major axis length). R-total is -0.65. Small R represents aggregates with approximate ellipsoid shape and larger R is spherical shapes. Aggregates become more ellipsoid with strong ε.

3.4 Size spectrum

Section 3.2 showed the direct influences of turbulence on aggregates by comparing averaged particle size and AR to averaged turbulence intensity. In this section, all data were used to compute the size distributions without taking averages. After computing the size spectrums, two regression lines were fitted (Fig.1-10). Slope1 was approximately -2 in all dataset, while slope2 was approximately -4 with ranges between -1.5 to -2.5 and -2.5 to -5.5, respectively (Table1-5 and Table1-6). The Kolmogorov scales were estimated from the average dissipation rate ε of each observation site and expressed with the red lines in Fig. 1-10. The intersections of slope1 and slope2 occurred nearly at the Kolmogorov scale length. These intersections were consistent with the peaks of nVd spectrums (Fig. 1-11). nVd significantly decreased after reaching these peaks. Thus, it is reasonable to consider that slope1 showed spectrums of particles undergoing the aggregation process while slope2 showed spectrums of disaggregated particles. The disaggregation occurred due to turbulence as the intersections appeared nearly at the Kolmogorov scale length.

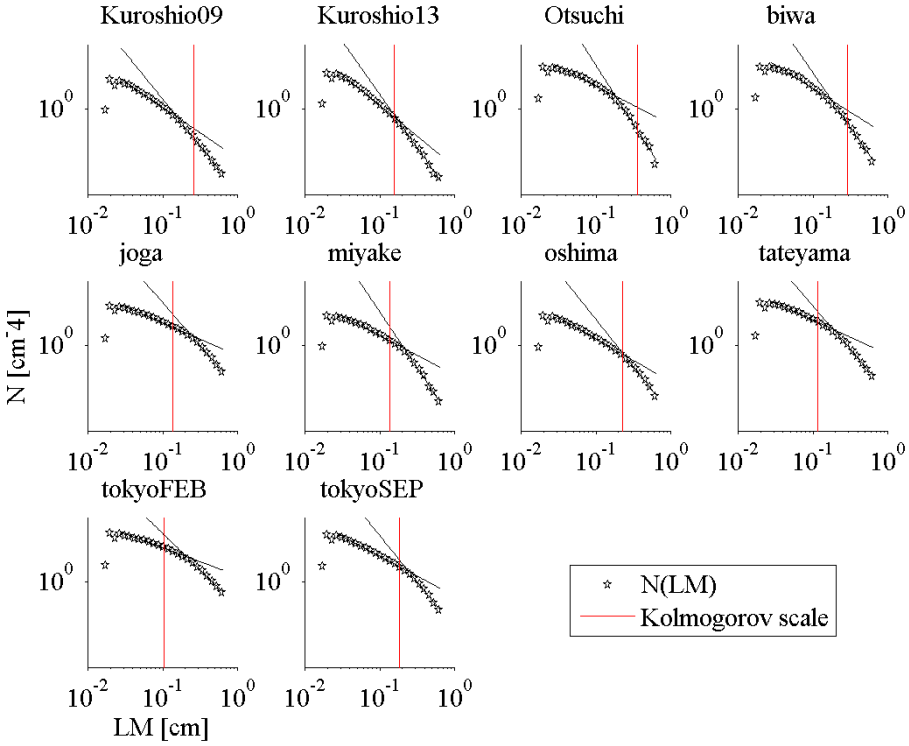

Figure 1-10 Size spectrum
Red lines indicate Kolmogorov scale length. All size spectrums have two slopes. Change from slope1(smaller size) to slope2(larger size) occurs almost at Kolmogorov scale. Slope1 approximates to -2 and slope2 approximates to -4;. Therefore Slope represents aggregation processes whereas slope2 represents disaggregation process.

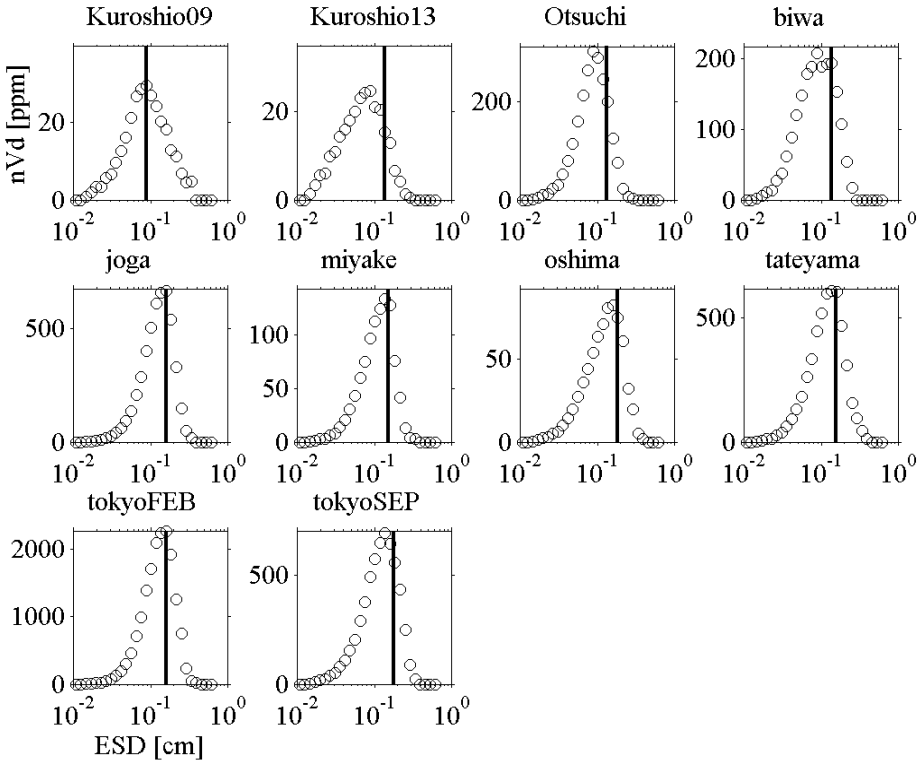

Figure 1-11 nVd spectrum
The black lines indicate the intersections of slope1s and slopes of size spectrums. The peaks of nVd spectrums met the intersections of slope1s and slope2s.

Table1-5 Size spectrum slopes

	Slope1	Slope2
Kuroshio 09	-2.38	-4.33
Kuroshio 13	-2.87	-4.96
Otsuchi	-1.80	-5.48
Biwa	-2.20	-5.08
Joga	-1.52	-4.00
Miyake	-1.83	-5.22
Oshima	-2.02	-4.39
Tateyama	-1.60	-4.04
Tokyo Feb	-1.30	-3.39
Tokyo Sep	-1.86	-4.31

Table1-6 Size spectrum depth intervals slopes

	Kuroshio 09		Kuroshio 13		Otuchi		Biwa		Joga	
	Slope 1	Slope 2	Slope 1	Slope 2	Slope 1	Slope 2	Slope 1	Slope 2	Slope 1	Slope 2
10-20	-2.64	-15.68	-3.31	-5.66	-2.06	-5.10	-1.77	-4.72	-1.53	-3.81
20-30	-2.36	-4.02	-3.26	-5.40	-1.76	-5.07	-1.71	-4.39	-1.56	-3.60
30-40	-2.54	-3.76	-3.10	-4.73	-1.73	-4.29	-2.51	-5.85	-1.41	-3.81
40-50	-2.64	-6.63	-2.71	-5.09			-2.43	-5.06	-1.38	-3.74
50-60	-2.34	-4.28	-2.50	-5.30			-2.52	-6.36		
60-70	-2.49	-4.96	-2.40	-5.50			-2.30	-5.85		
70-80	-2.51	-4.96	-2.41	-4.74			-2.38	-6.11		
80-90	-2.41	-5.11	-2.52	-4.90			-2.19	-5.35		
90-100	-2.63	-4.94	-2.69	-5.27			-2.26	-4.35		

	Miyake		Oshima		Tateyama		Tokyo Feb		Tokyo Spe	
	Slope 1	Slope 2	Slope 1	Slope 2	Slope 1	Slope 2	Slope 1	Slope 2	Slope 1	Slope 2
	-1.85	-4.38	-2.16	-3.51	-1.90	-5.45	-1.22	-3.53	-2.04	-3.66
	-1.94	-5.61	-2.11	-4.32	-1.53	-3.92	-1.32	-3.28	-1.89	-4.25
	-1.95	-5.70	-2.19	-4.52	-1.94	0.00	-1.29	-3.39	-1.94	-4.84
	-1.99	-6.37	-1.81	-4.10			-1.30	-3.00	-1.90	-4.33
	-1.83	-5.28	-1.59	-4.44			-1.11	-2.17	-1.67	-4.01
	-1.83	-4.90	-1.64	-3.87						
	-1.69	-4.44								
	-1.48	-3.84								
	-1.68	-4.46								

4. Conclusion

Past studies suggested the importance of turbulence in aggregation and disaggregation processes of marine aggregates by laboratory experiments and theoretical studies (Colomer, et al., 2005; Jackson, et al., 1995). However, no study has shown the evidence of the turbulence-aggregation theory using *in-situ* observation data, because aggregates are too fragile to survive during typical bottle sampling methods. Utilising a Digital Still Logger camera with TurboMAP-L that carries multiple probes to measure physical and biological parameters enabled us to collect images of aggregates, hydrographic background and microstructures simultaneously.

The comparison between mean ε and mean MAL showed that aggregates were undergoing the aggregation process until turbulence reached the critical point, $\varepsilon=10^{-6}Wkg^{-1}$(Fig.1-8). Large stretched aggregates are formed during this process. The ε

remains smaller than $10^{-6}Wkg^{-1}$ throughout the wide range of the world's oceans. Therefore the turbulence-aggregation mechanism which was observed in this study could be a worldwide phenomenon.

Although this comparison did not have enough data sets to explain the disaggregation process, data for non-averaged size spectrums showed the distributions of disaggregated particles. The slopes of size spectrums were consistent with the results of many previous studies, showing slopes of size spectrum range between -2 and -6 (Jackson & Checkley Jr, 2011; Guidi, et al., 2009; Stemmann, et al., 2008). The shifts from slope1 to slope2 occurred nearly at the Kolmogorov scale length in this study. This suggested that slope1 shows distributions of particles undergoing the aggregation process and slope2 shows distributions of disaggregated particles.

This study demonstrated the strong influences of turbulence on the aggregation and the disaggregation processes. As the contributions of aggregates to export production and associated biogeochemistry are considered to be important, the impacts of turbulence through the aggregation and disaggregation processes on the world's marine ecosystems could be also substantial.

Chapter 3: A comparative study of digital holographic systems and a digital still camera: in-situ marine aggregate observations

Abstract

Flocculated suspended particles consisting of organic and inorganic matter called marine aggregates or marine snow widely exist in marine environments.
The *in-situ* observation study using a Digital Still Logger camera(DSL camera) and a microstructure profiler, TurboMAP-L, demonstrated the clear relationship between turbulence and aggregation mechanisms. However, DSL camera was not able to resolve the detailed features of captured aggregates. In this study, inline digital holographic systems were simultaneously deployed with TurboMAP-L during a field campaign. A microstructure holographic system (MSS-HOLO, Marine lab, Plymouth Univ.) and LISST-HOLO (Sequoia Scientific Co.) were prepared. Both MSS-HOLO and LISST-HOLO successfully captured clear images of marine aggregates. Although holographic systems resolved clear images of aggregates, there were significant differences in particle abundance (aggregates ≥1mm) between holographic systems and DSL. DSL measured 1.5 times more aggregates ≥ 1mm than that of LISST-HOLO and 7 times more than MSS-HOLO. Size spectrum analysis suggested that holographic systems destroyed fragile aggregates due to the disturbances caused by their deployment method.

1. Introduction

Flocculated particles involving organic and inorganic matter are commonly known as marine snow or aggregates. Their size can be as large as possible and may exceed 1m (Puskaric, 2012). Increase in particle size by flocculation accelerates sinking speed (Laurenceau-Cornex, et al., 2015). Therefore the contribution of marine aggregates to the biological pump or material transport to the deeper ocean is significantly large(Puskaric, 2012; Flower & Knauer, 1986; Kindler, et al., 2010; Riebesell, 1991). Food chains of small magnitude take place inside marine aggregates, thus living organisms inside the aggregates can obtain nutrients efficiently even in oligotrophic environments (Goldman, 1984). Internal food chain or external predation destroy the aggregates and leak organic matter. This leaked organic matter provides nutrients to the ambient waters. This process is important not only in nutrient supply but also attracting more zooplankton and bacteria (Kiørboe, 2001). It is clear that marine aggregates play important roles and that more detailed

studies of their dynamics are required to better understand their roles in marine ecosystems.

However, high proportions of transparent exopolymer particles (Chow, et al., 2015; Alldredge, et al., 1993; Bar-Zeev, et al., 2012) inside aggregates makes them extremely fragile. Therefore *in-situ* observation of aggregates by net or bottles are challenging. Some studies used scuba diving to collect aggregates without destroying them, however, the number of aggregates they could collect was limited (Puskaric, 2012; Alldredge & Gotschalk, 1988). In Chapter 2, it was demonstrated that the in-situ observations we conducted captured numerous aggregates successfully. This study showed a clear and strong relationship between turbulence and aggregation mechanisms. However, the imaging device used in Chapter2, the DSL camera, did not resolve the detailed structures of aggregates. In Chapter 3, the detailed structures of aggregates were clearly observed by utilising the new image recording technology, inline holographic systems.

2. Methods

2.1 Observation site

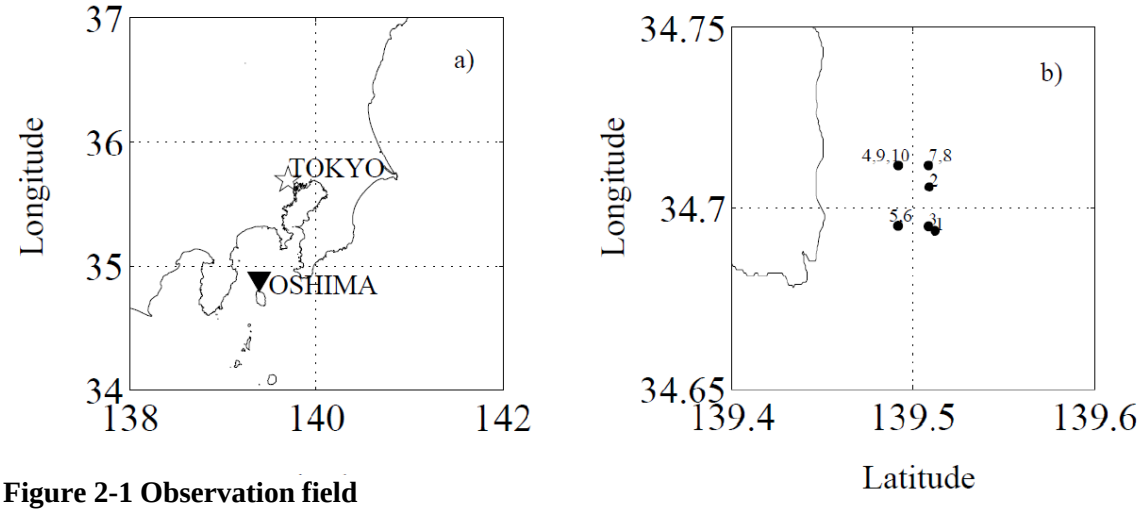

Figure 2-1 Observation field
a) Location of Oshima island b) deployment site

A time series campaign was conducted on 22nd of June 2013 offshore southeast of Oshima Island (Fig2-1, Table2-1), Tokyo Japan, using R/V Seiyo-Maru of Tokyo University of Marine Science and Technology. Seven instruments were deployed during this campaign; a microstructure holographic system (MSS-HOLO), a digital holographic particle imaging system LISST-HOLO, a particle size and volume distribution analyser LISST100-X, a Digital Still Logger camera (DSL), two RINKO

profilers , and a microstructure profiler TurboMAP-L. Three independent systems were built out of these seven instruments; (i) RINKO profiler with MSS-HOLO, (ii) RINKO profiler, LISST-HOLO, LISST-100X mounted on a single frame (iii) DSL camera mounted on TurboMAP-L. During 15 hours of observation, we conducted 10 sets of deployment for each system.

Table 2-1 Observation details

Cast	Time	Longitude	Latitude	Maximum Depth [m]			Image number		
				MSS-HOLO	LISST-HOLO	DSL (TML)	MSS-HOLO	LISST-HOLO	DSL
1	18:16	34.6937	139.512	48.8	No Data	No Data	1858	66	No Data
2	19:49	34.7058	139.509	39.8	No Data	51.6	1169	88	647
3	21:21	34.6949	139.508	46.5	50.6	53	2796	95	626
4	22:49	34.7117	139.492	36.8	51.5	53.1	1077	66	647
5	0:43	34.695	139.492	51.7	28.7	57.9	2047	97	684
6	1:58	34.6949	139.492	51.4	52.1	54.7	1811	84	726
7	3:16	34.7117	139.508	51.5	51.1	59.8	1738	83	683
8	4:47	34.7117	139.508	49.9	No Data	No Data	1331	51	No Data
9	6:20	34.7118	139.492	52	50.4	No Data	974	65	No Data
10	7:47	34.7117	139.492	48.3	No Data	No Data	2064	133	No Data

2.2 Holographic systems

2.2.1 Instruments

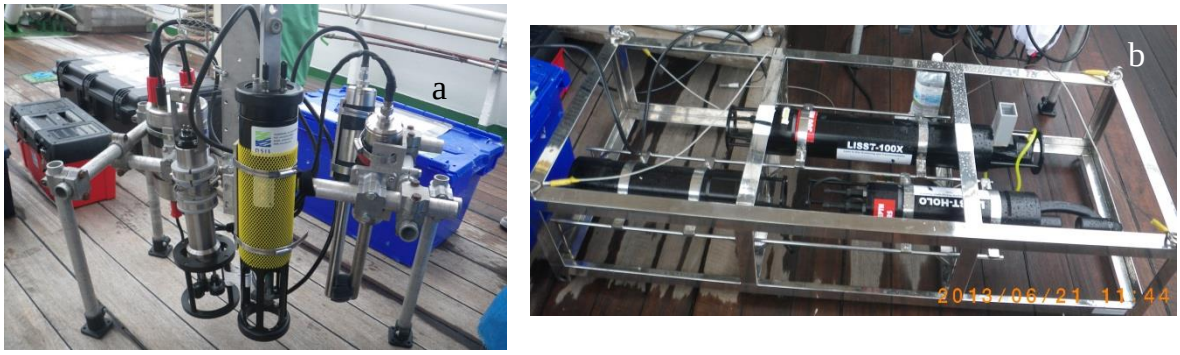

Figure2-2 Holographic systems
MSS-HOLO and RINKO profiler b) LISST-HOLO, LISST100X and RINKO profiler

Table2-2 Imaging devices specifications

	MSS-HOLO	LISST-HOLO	DSL
Image resolution [μm]	11.5	25	120
Sample volume [mm^3]	451	780	8000
Field view [mm×mm]	5.2×3.5	7.0×5.3	20×20
Camera depth [mm]	25	29	20
Pixel size [μm]	3.4	4.4	59
Sampling speed [Hz]	5	1	5

Two different types of holographic systems, the microstructure holographic system (MSS-HOLO) and LISST-HOLO, were used (Fig. 2-2). MSS-HOLO was developed by Prof. Nimmo Smith of Plymouth University for in-situ particle observations and LISST-HOLO is a commercial holographic system, manufactured by Sequoia Scientific with support from Prof. Nimmo Smith (Loomis, 2011). As presented in Table 2-2, MSS-HOLO has higher resolution and a sampling speed but a smaller sampling volume than LISST-HOLO. The number of images recorded for each deployment depends on the depth as well as the sampling speed.

2.2.2 Deployment

MSS-HOLO and LISST-HOLO record three dimensional holographic images which enable us to accurately measure the size of particles and distances between particles. Both systems were lowered by onboard winch. The deployment speed was $0.1ms^{-1}$ for MSS-HOLO and $1ms^{-1}$ for LISST-HOLO. MSS-HOLO observation was operated by a computer onboard and obtained image data were transmitted and recorded on the computer. LISST-HOLO recorded images in an internal memory stick. Although both systems are designed to measure physical parameters of sampling water such as depth, temperature and conductivity as well as taking images, LISST-HOLO had a technical problem and did not record the depth. Therefore the depth data obtained by RINKO profiler that was mounted on the same frame was used.

2.2.3 Data processing

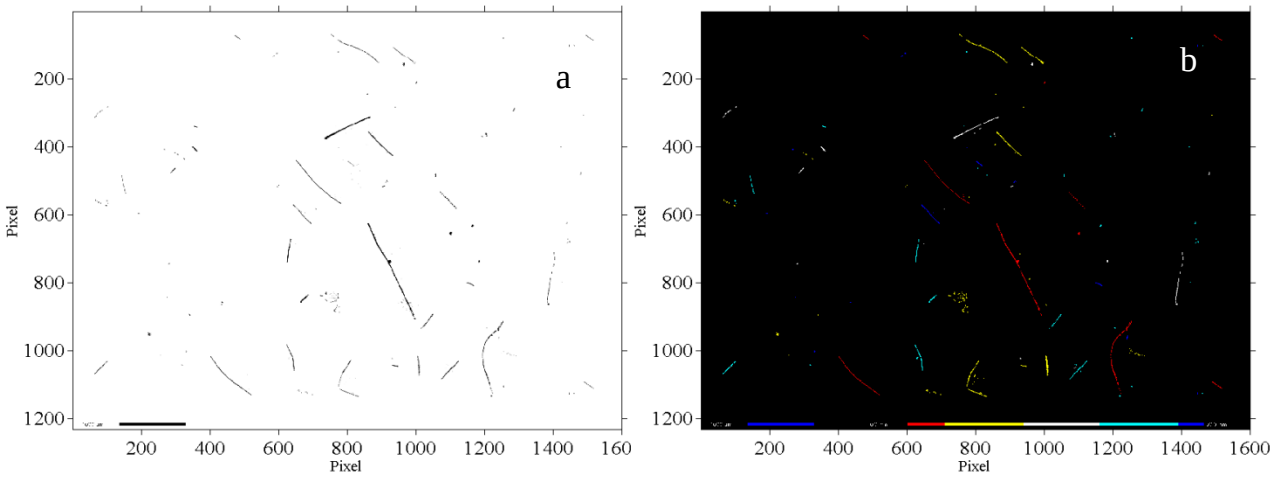

Figure 2-6 Reconstructed holograms
a) Reconstructed holographic image b) particles depth indicator

Particles in the sampling volume diffract a coherent laser beam which is derived from one side. The diffracted laser beams and collimated laser beams create interference patterns on the Charge- Coupled Device (CCD) image sensor at the other side (Graham & Nimmo-Smith, 2010). The device records these interference patterns as holograms. These interference patterns contain phase and amplitude which indicate the distance from the camera and the size of the particle.
Recorded holograms are digitally reconstructed to bring measured objects into focus using the software HOLO Batch. HOLO Batch was developed by Sequoia Scientific Inc. for hologram reconstruction use. A simplification of convolution approach is used for reconstruction (Graham, et al., 2012; Owen & Zozulya, 2000). It is designed to run on MATLAB (The Mathworks Inc., Natick, MA, USA). During the reconstruction process, HOLO Batch extracted particle properties using MATLAB function *regionprops*(Table2-3).

The holograms have a z-axis as they are three dimensional images. The resolution in z-axis is arbitrary. As higher resolution provides clearer images in two dimensions, setting smaller step size in the z-axis provides reconstructed images with higher quality. In this study, step size was set to 0.195mm, generating 128 slices for each holographic image.
At the end of the reconstruction process, a black and white montage image which shows all in-focus particles and an image indicating the distance of each particle from the camera by colour were generated(Fig. 2-3).

In order to extract aggregates, a threshold value was set by using, $R = \frac{\mathrm{Area_{convec}}}{\mathrm{Area\ _{total}}}$ where $\mathrm{Area_{total}}$ is the total area of particles and $\mathrm{Area_{convex}}$ is the area of the particle excluding cavities. The ratio R expresses solidity of particles in a range between 0 and 1; R≈0 is extremely porous and R≈1 is almost solid. In this study, particles are separated into aggregates and residual particles at R=0.5.

Table2-3 Particle properties

	MSS-HOLO	LISST-HOLO	DSL
Major axis length	✔	✔	✔
Minor axis length	✔	✔	✔
Equivalent sphere diameter	✔	✔	✔
Area	✔	✔	✔
Convex area	✔	✔	
Volume	✔	✔	
Coordinate	✔	✔	
Camera depth	✔	✔	

2.3 LISST 100X

LISST 100X was used to measure particle size distribution and the volume concentration simultaneously with LISST-HOLO (Fig.2-2). In addition to particle size and volume distribution, it also recorded other parameters such as pressure, temperature and optical transmission. The LISST 100X had a technical problem on the pressure sensor and failed to measure pressure data. Therefore depth data from RINKO profiler was used instead.

LISST 100X can detect particle sizes ranging between 2.5μm and 500μm. Data were recorded in a built-in memory stick and the system was powered by battery as with LISS-HOLO. The size bins were defined as follows:

$$2.50 \times (200^{\frac{1}{32}})^{i}, \text{ where } i \text{ is from 0 to 31} \quad \text{Eq.(2-1)}$$

2.4 RINKO profiler

Table2-4 RINKO profiler specifications

Parameters	Range	Accuracy	Resolution	Sampling rate [Hz]
Depth [m]	0 to 600	±0.3%	0.01m	5
Temperature [degC]	-3 to 45	±0.01	0.001	5
Conductivity [mS/cm]	2 to 70	±0.01	0.001	5
Salinity [PSU]	2 to 42	±0.01	0.001	5
Dissolved Oxygen [mg/L]	0 to 20	±2%	0.001	2.5
Chlorophyll [ppb]	0 to 400	±1%	0.01	5
Turbidity [FTU]	0 to 1	±0.3	0.03	5

Physical parameters for MSS-HOLO and LISST-HOLO were measured simultaneously using RINKO profilers (JFE Advantech Co., Ltd.). RINKO profiler carries a pressure sensor, a fluorescence sensor, a turbidity sensor, a conductivity sensor, and a dissolved oxygen sensor (table2-4). A RINKO profiler was mounted on a single frame with MSS-HOLO. Another RINKO profiler was mounted on another single frame with LISST-HOLO and LISST-100X. It is battery powered and data is recorded to 1GB in-built memory. The body length is 49.1cm and weight in water is 1.0 kg. The compact body size did not change the weight balance of either MSS-HOLO or LISST systems.

2.5 TurboMAP-L and DSL

2.5.1 TML

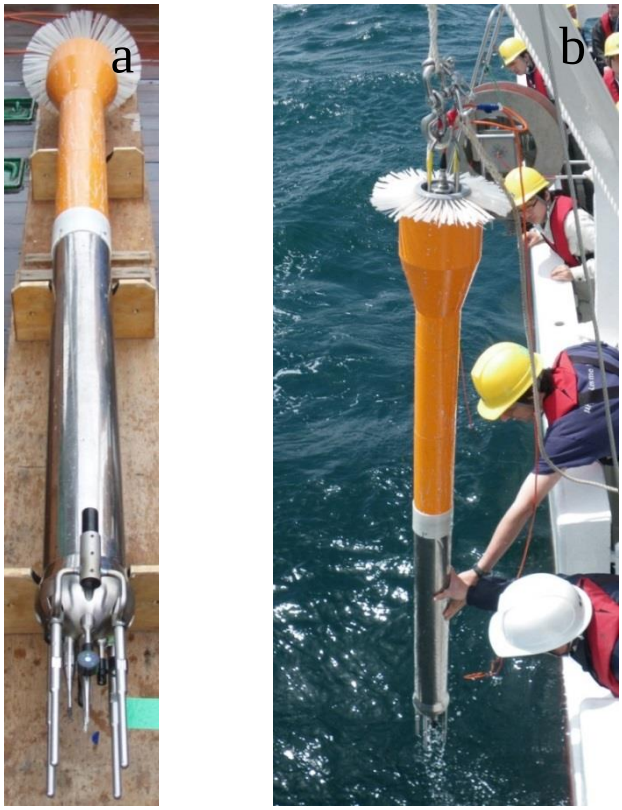

Figure 2-4 TurboMAP-L
a: TurboMAP-L
b: TML deployment in free fall mode. Recovery is controlled by the winch.

Table 2-2 TML specification

Parameters	Range	Accuracy	Resolution	Sampling rate [Hz]
Shear[s^{-1}]	0 to 4	5%	0.0001	512
Fast temperature[degC]	-5 to 45	±0.01	<0.0001	512
Slow temperature[degC]	-5 to 45	± 0.05	0.001	64
Conductivity[mS^{-1}]	0 to 70	± 0.01	0.002	64
Pressure [m]	0 to 500	0.2%	0.01	64
Accelerometers[G]				
X				256
Y	±1	1%	0.0005	256
Z				64
Fluorescence				
LED [ugL^{-1}]	0 to 100	±0.5	0.005	256
Laser				256
Turbidity[ppm]	0 to 100	±1	0.0005	256

For biological and physical parameter measurements, we utilised a microstructure profiler, TurboMAP-L (TML) which carries a pressure sensor, laser and LED fluorescence sensors, a turbidity sensor, a conductivity sensor, a high accuracy temperature probe and a high resolution temperature probe , and two shear probes (Table2-2 and Fig.2- 2) (Doubell, et al., 2009). The profiler utilises on board power and data for each parameter is collected at 64 – 512 Hz. Collected data is transmitted through the cable to a connected computer on the vessel. During the deployment, the instrument is in freefall mode, which does not disturb sampling objects or ambient conditions by the instrument. The most significant feature of this instrument is that it carries two fluorescence probes, LED and laser, which are different in their spatial resolution and sampling volume. The LED fluorescence probe is able to measure a larger sampling volume at 2 cm scale resolution whereas the laser fluorescence probe resolves 2mm scale fluorescence in a smaller sampling volume. Doubell, et al., (2009) showed that the laser fluorescence probe detected locally high signals, although 1 metre scale averaged data of laser fluorescence and LED fluorescence showed no difference between the two probes. Doubell et al.,(2009) hypothesized that the locally high laser fluorescence signals are resolved marine aggregates.

2.5.2 Turbulent kinetic energy dissipation rate (ε)

The rate of turbulence kinetic energy dissipation, ε, was estimated from the shear data, assuming isotropic turbulence. The following isotropic formula was used to estimate ε (Eq.2-2). The minimum eddy scales, the Kolmogorov length scale ($\lambda\varepsilon$), was also calculated by equation2-3.

$$\varepsilon = \frac{15}{2}\nu\overline{\left(\frac{\partial u'}{\partial z}\right)^2} \quad \text{Eq.}(2-2)$$

$$l_k = \left(\frac{\nu^3}{\varepsilon}\right)^{\frac{1}{4}} \quad \text{Eq.}(2-3)$$

ν is kinematic viscosity coefficient, u’ is horizontal velocity, z is vertical coordinate. In this study, ε was estimated by integrating power spectrums over 2 second data segment. In order to avoid integration of the mechanical noise as well as electric noise, spectrum were integrated over the wavenumber range where Nasmyth empirical spectrum matched with that from the measurements. The lost shear variance in these noise wavenumber ranges, was recovered by integrating Nasmyth spectra (Nasmyth, 1970; Oakey & Elliot, 1982).

2.5.4 Digital Still Logger camera

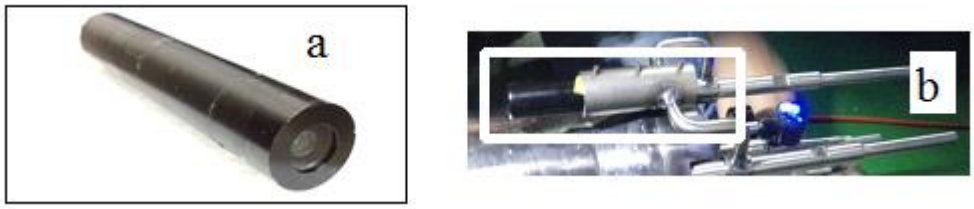

Figure 2-5 Digital Still Logger camera
a : A Digital Still Logger Camera
b : DSL camera mounted on TML using an aluminium frame, facing the direction of travel. LED fluorescence probe is used for light source. As the light source is weak, the observations were conducted only during night time.

The Digital Still Logger camera system (DSL camera; DSL 190-VDT2, Little Leonardo Co.) was originally developed for marine mammal research purposes. DSL camera is 2.2cm in diameter, 11.9cm in body length. Its field view is 6×7.5 cm with 59µm per pixel (Table2-3, Fig.2-3). Although the DSL camera carries temperature and pressure sensors, TML depth data was used in order to more accurately measure the depth.

DSL camera was mounted on TML using a special aluminium frame to collect images in the direction of its travel. The LED light from the fluorescence probe was used as the DSL camera light source. The LED probe utilises 6 LEDs that intersect 15 mm away from the surface of the probe. Focal depth of DSL is 10 cm and DSL was mounted on the TML to capture this LED intersection in its focus. As the LED light source was weak, the observations were performed only during night time to prevent light disturbance from sunlight. Sampling speed was 5Hz, collecting 1 frame every 10 cm. All the pictures were compressed and recorded in the internal memory, data transmission was performed manually each time the DSL camera was recovered.

2.5.3 DSL image process

As described in Doubell et al. ,(2009), the following operations were performed for analysis of DSL images. Firstly images were cropped to 340 × 340 pixels where LED light is projected most strongly and blue colour band was extracted (Fig.2-5 a and b). Unequal distance from the light source over the image field creates non-uniform illumination across the image. To normalise the imbalance of illumination, the intensity of each image was divide by the background image. The background image was generated by average of all images in each deployment after applying a 15 × 15 pixel filter (Fig. 2-5 c). Threshold was defined by discrimi-

nant analysis method and computed binary images (Fig. 2-5 d). Individual particle properties such as major and minor axis length, equivalent spherical diameter and area were determined by MATLAB *regionprops* function (The Mathworks Inc., Natick, MA, USA). Particle volume was estimated from the equivalent spherical diameters. To separate aggregates and individual plankton cells, only particles having a 5 or more pixel area were extracted as aggregates making aggregate resolution 120µm. Following the methods described in Doubell, et al., (2009), Franks & Jaffe (2001), Franks & Jaffe(2008), all the particles were screened whether they were in focus. Finally, any unclear images were ignored by visual inspections.

2.6 Size spectrum

The number of particles in each bin class was counted to determine size spectrums. Lognormally increasing bin classes (d) were computed by equation 2-4. The normalised number of particles (n) was computed by counting the number of particles with major axis length (MAL) in each bin class, then dividing them by Δd. The number of particles was plotted against d to express the size spectrum.

$$d = 10^{(2+0.065\times i)}, i=1 \text{ to } 28, \qquad \text{Eq.(2-4)}$$

Particles < 300 µm were ignored as mechanical noise in regression lines fittings. Two regression lines were fitted to each size spectrum.26 cases were tested to find the best fit. First slope (Slope1) was fitted to 1st to j-th bins spectrum, and second slope (Slope2) was fitted to j-th to end, where j=2 to 27. Nf is the theoretical value computed by fitting. Rss was calculated for each case (Eq.2-5). The fit that had the least Rss was defined as the best fit.

$$R_{ss} = \sum_{1}^{92} (N_j - Nf_i)^2 + j=1 \text{ to } 92 \qquad \text{Eq.(2-5)}$$

3. Results and discussion

3.1 Hydrographic background

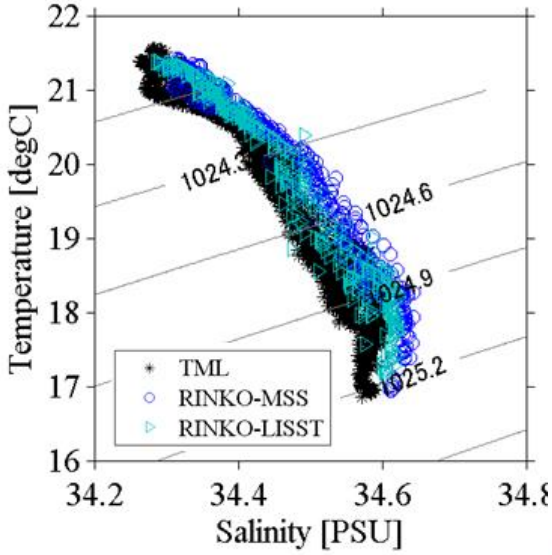

Figure 2-7 TS diagram
Stars indicate TurboMAP-L (DSL)
Circles indicate RINKO on MSS-HOLO
Triangles indicate RINKO on LISSTsystem

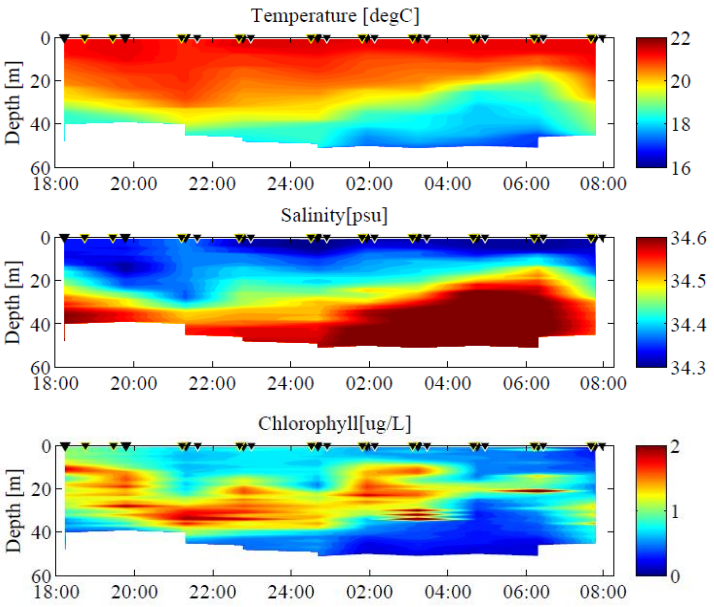

Figure2-7 Hydrographic contour
Time series hydrographic background. Cold water intrusion and chlorophyll-a layered structure are observed

A TS diagram showed similar water properties consistency among the three systems; two holographic systems and the DSL camera (Fig.2-6). Although they were deployed independently, the three systems observed nearly same water mass. According to Hanawa and Mitsudera (1987) the Kuroshio water shows salinity between 34 and 36 and temperature ranges between 18 and 22 degrees. Thus observed water mass represents features of the Kuroshio current water mass. Throughout the observation, the rate of turbulent kinetic energy dissipation (ε) did not exceed 10^{-6} $Wkg^{-1}$and likely remained 10^{-8} Wkg^{-1}. Cold water intrusion by internal tide was observed after midnight(Fig.2-7).

3.2LISST100X

Particle abundance measured by LISST100X, indicated that particles smaller than 200μm have high population at this observation site (Fig, 2-8). Particle abundance maxima appeared between 20-40 metres depth where chlorophyll-*a* concentrateon and turbidity maxima were measured.

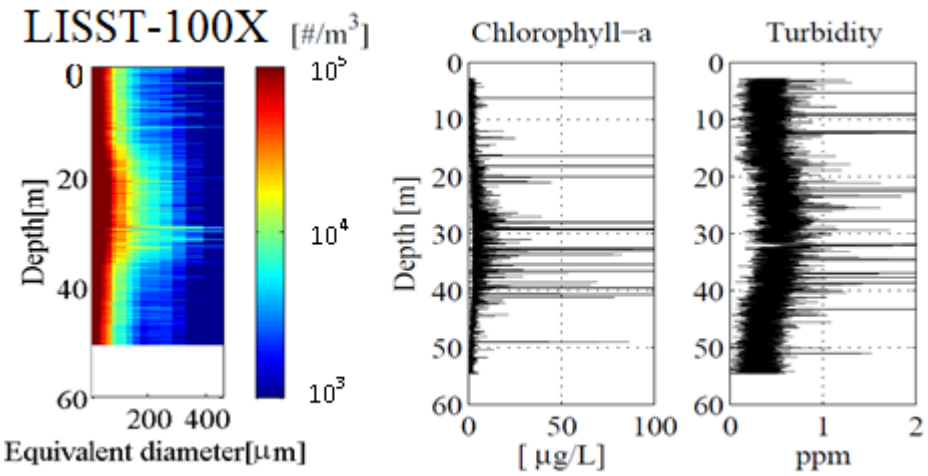

Figure 2- 8 LISST100 X
Left) LISST-100X particle abundance. Colours indicate particle abundance and x axis indicates size.
Middle) Chlorophyll-a abundance – TurboMAP-L
Right) Turbidity – TurboMAP-L

3.3 Particle images

Both holographic systems captured the details of aggregates; MSS-HOLO images were clearer than those of LISST-HOLO . (Fig 2- 9 a and b). Although LISST-HOLO resolution is coarser than MSS-HOLO, the resolution was sufficient to identify aggregates.

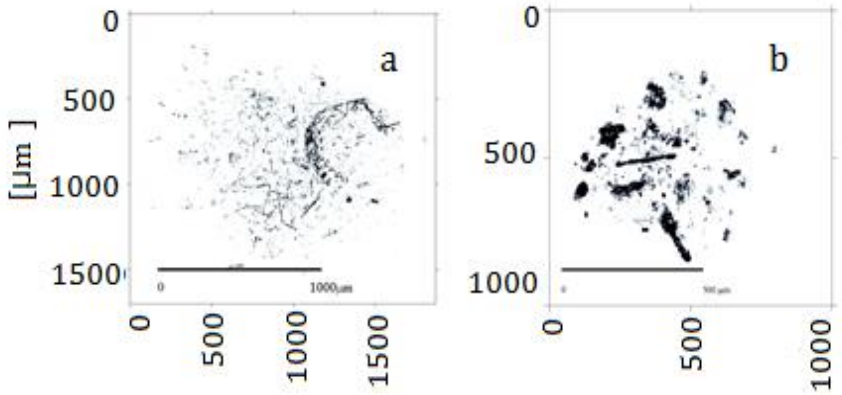

Figure 2-9 Aggregate images
a:Aggregate image from MSS-HOLO
b:Aggregate image from LISST-HOLO

3.4 Particle abundance

MSS-HOLO measured the smallest abundance of both total aggregates and large aggregates (aggregates ≥ 1mm). LISST-HOLO measured a slightly larger number

of aggregates than that measured by the DSL camera. This is reasonable as the resolution of LISST-HOLO is higher than DSL. However, DSL measured almost 1.5 times more large aggregates (aggregates≥1mm) than LISST-HOLO. Between MSS-HOLO and DSL this difference reaches 7-fold.

Table2-6 Particle abundances

	MSS-HOLO		LISST-HOLO		DSL	
	Number	# / m^3	Number	# / m^3	Number	# / m^3
Aggregate ≥ 1mm	138	0.18×10^5	60	0.93×10^5	17803	1.46×10^5
Aggregates	38812	5.06×10^5	6837	10.56×10^5	106713	8.74×10^5

3.5 Size spectrums

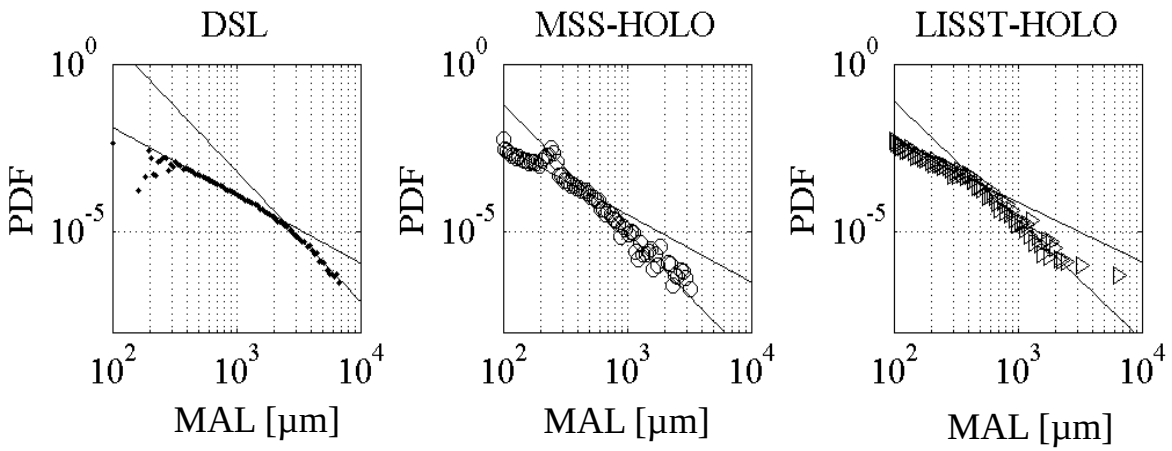

Figure 2-10 Size spectrum
Slope1 approximates to -2 and slope2 approximates to -4. Changes from slope1 to slope2 occur at about 2mm, 0.5mm and 0.2mm

Table 2-7 Size spectrum slopes

	Transit point [μm]	Slope1	Slope2
DSL	2426	-2.03	-3.9
MSS	513	-2.02	-3.83
LISST	298	-1.78	-3.58

Two slopes were fitted for each size spectrum (Fig.2-10). The each slope ranged between -2 and -4 (Table2-7); slope1 was approximately -2 and slope2 was approximately -4. This result was consistent with the results from previous studies which showed slopes of size spectrums in the range between -2 and -6 (Li, et al.,

2004; Flower & Knauer, 1986; Burd, 2013; Stemmann, et al., 2008; Renosh, et al., 2014).

The slopes of size spectrum in aggregates have been shown to be highly dependent on their aggregation mechanisms (Li, et al., 2003; Burd & Jackson, 2002). These studies showed that the gradient of slopes approximates to -4 when turbulence is controlling the size distributions through theoretical and experimental investigations. In Chapter2, the DSL camera results indicated that slope1 represented the aggregation process while slope2 represented the disaggregation process. The each slope was estimated to be approximately -2 and -4, respectively, which are consistent with the results here. The result in Chapter2 also demonstrated that the intersection of slope1 and slope2 occurred approximately at the Kolmogorov scale. Assuming that each intersection appeared at the Kolmogorov scale, the rates of turbulence kinetic energy dissipation which each instrument underwent were estimated. From the intersection scale, it can be speculated that both holographic systems should have undergone strong turbulence, with the maximum ε (MSS-HOLO) $\approx 10^{-5}$Wkg^{-1} and ε (LISST-HOLO) $\approx 10^{-4}$Wkg^{-1}, whereas ε (DSL camera) was estimated to be $\approx 10^{-8}$Wkg^{-1}. The ε observed during this observation was 10^{-8}Wkg^{-1} on average and did not exceed 10^{-5}Wkg^{-1} with average 10^{-7}Wkg^{-1}. The Kolmogorov scale is 2292μm when ε is 10^{-7}Wkg^{-1}. Therefore, the intersection scale of DSL showed the consistent result with the estimated Kolmogorov scale, whereas holographic systems showed much smaller scale of the intersections. Nevertheless, although the TS diagram showed that the three instruments observed approximately the same water mass, ε values estimated from the intersection of slopes were inconsistent. This is probably due to the different deployment methods.

DSL was deployed in free fall mode and observed undisturbed water. In contrast, the holographic systems were lowered by the on-board winch. During the deployments, the holographic systems received sudden momentary upward motions because of the upset of the boat. This upward motion reached 1ms^{-1}. The Reynolds number where U=1ms^{-1} and L=2.5mm and 2.1mm (the distances between the lasers and their respective sensors) were greater than 2×10^{4}. This extremely large Reynolds number indicated that the holographic systems should have disturbed water strongly.

Since the water was disturbed by the systems, fragile aggregates were hypothesised to be destroyed. Another possible explanation is that in addition to destroying the aggregates, the upward motions during deployments may have created complex vortices around the sampling volume. These complex vortices made it physically difficult for aggregates to reach the sampling volume.

4.Conclusion

Two holographic systems successfully resolved the detailed structures of aggregates. Although the resolution of LISST-HOLO is lower than MSS-HOLO, it was sufficient enough to resolve clear structures of aggregates. Since LISST-HOLO is a commercial product, this success can be a significant improvement for the in-situ observations of marine aggregates. However, the results of particle abundance and size spectrums suggested the risks of observations using holographic systems too. The current deployment methods may have destroyed aggregates during deployment or physically diverted aggregates. In order to verify these hypotheses, developing an observation method that enables free fall mode observations with LISST-HOLO is necessary.

Chapter4 Conclusion and future prospective

Chapter2 describes the fieldwork, which was conducted in an attempt to demonstrate the influences of turbulence on aggregation mechanisms using *in-situ* observation data. Strong correlations were observed between aggregates total volume concentrations and turbidity as well as ILFI. nVd spectrums analysis verified that the DSL camera successfully collected images of aggregates.

The strong correlation between mean major axis length (MAL) and the rate of turbulent kinetic energy dissipation, ε, as well as the comparison of the aspect ratio AR with ε demonstrated that turbulence clearly promotes the growth of aggregates. This result also showed that aggregates become more stretched the stronger turbulence becomes.

The comparison between mean ε and mean MAL showed that there were few particles exceeding 1mm in size. The scale of 1mm is the Kolmogorov scale length, the smallest eddy scale, when ε is 10^{-6}Wkg^{-1}. These results suggest that particles undergo the aggregation process under the condition of $\varepsilon < 10^{-6}$Wkg^{-1} and above which disaggregation process by turbulent shear erodes larger aggregates than 1 mm. Although the data set was not sufficient to prove the occurrence of the disaggregation process from this comparison, size spectrum clearly distinguished between the aggregation process and the disaggregation process. All the non-averaged MAL data were used to describe the size spectrum. Two fitted regression lines for each size range showed a clear difference between their slopes. The regression line fitted to the larger aggregates were much steeper than the ones fitted

to the smaller aggregates. The intersections of slope1 and slope2 occurred nearly at the Kolmogorov scale. These results suggest that slope1 showed the aggregation processes while slope2 showed the disaggregation processes, supporting our hypothesis that turbulence controls the aggregation and disaggregation processes. The intensity of ε remains smaller than 10^{-6}Wkg^{-1} in the typical marine environment. Only near the surface and bottom boundary layers show extremely large values $\varepsilon > 10^{-3}$Wkg^{-1}. Therefore, the aggregation process that turbulence promotes is likely to be ubiquitous. This study demonstrated the importance of turbulence in the aggregation process using *in-situ* observation data while past studies were based on either theoretical or laboratory experiments (Colomer, et al., 2005; Serra, et al., 2008). Assuming that this is a worldwide phenomenon, this study was a very important step to explain the contribution of turbulence to marine aggregate, export production, biological pump, and marine ecosystems.

Chapter 3 showed that *in-situ* observations of aggregates using the inline digital holographic systems were potentially successful with respect to resolving the details of aggregate structures. LISST-HOLO provided clear images of aggregates. As LISST-HOLO is a commercial product, future studies of aggregates using the LISST-HOLO will be able to provide more information on the nature of aggregates. However, comparative studies between holographic systems and DSL camera showed that holographic systems may not be measuring aggregates accurately. Despite the TS diagram showing that the three instruments measured nearly the same water mass, size spectrum suggested that the holographic systems were subject to extremely strong turbulence while DSL camera did not show such a result. The Reynolds number indicated an unstable water condition; therefore, it can be plausible that the holographic systems destroyed the many aggregates. The behaviours of holographic systems during the deployments were not as smooth as those of the DSL camera. This was because of the different deployment methods. The holographic systems were controlled by winch, whereas DSL camera was in freefall mode. In order to verify whether deployment methods have an influence on the observation results and to enable more accurate measurements, improving deployment methods is required.

Acknowledgements

I thank Dr. Nimmo Smith and Dr. Fukuda for providing holographic systems used in this study. A special ‘thank you’ to Dr. Graham, who joined the cruise in 2013 and operated the holographic systems overnight.

My Master's education and thesis works were guided and supported by my supervisor Professor Yamazaki, co-supervisor A/Professor Nagai, Dr.Nimmo Smith, Dr. Graham, Professor Jackson and all laboratory members. I appreciate all the training and help provided by them.
The big support from my family + three cats and the cheering from Singapore were of course encouraging. I really appreciate them, especially my parents, for understanding and giving me the opportunity to continue my study to PhD.

References

Alldredge, A. & Gotschalk, C., 1988. In-situ settling behavior of marine snow. *Limnology Oceanography,* Volume 33, pp. 339-351.
Alldredge, A., Gratana, T. & Citschalk , C., 1990. The physical strength of marine snow and its implications for particle disaggregation in the ocean. *Limnology and Oceanography,* 35(7), pp. 1415-1428.
Alldredge, A., Passow, U. & Logan, B., 1993. The abundance and significance of a class of large, transparent organic particles in the ocean.. *Journal of Plankton Research,* Volume 40, pp. 1131-1140.
Bar-Zeev, E., Berman-Frank , I., Girshevitz, O. & Berman, T., 2012. Revised paradigm of aquatic biofilm formation facilitated by microgel transparent expolymer particles. *PNAS,* 109(23), pp. 9119-9124.
Bochansky, A. B., Jericho, M. H. & Hernal, G. J., 2013. Development and deployment of a point-source digital inline holographic microscope for the study if plankton and particles to a depth of 6000m. *Limnology and Oceanography : Methods,* Volume 11, pp. 28-40.
Buesseler, K. & Boyd, P., 2009. Shedding light on prosesses that control particle export and flux attenuation in the twilight zone of the open ocean. *Limnology and Oceanography,* Volume 54, pp. 1210-1232.
Burd, A. B., 2013. Modeling particle aggregation using size class and size spectrum approaches. *Journal of Geophysical Research: Oceans,* Volume 118, pp. 3431-3443.
Burd, A. & Jackson, G., 2002. Modeling steady-state particle size spectra. *Environmental Science and Technology,* Volume 36, pp. 323-327.
Chow, J. S., Lee, C. & Engel, A., 2015. The influence of extracellular poly sacchrides growth rate and free cocoliths on the coagulation efficiency of Emiliania huxleyi. *Marine Chemistry,* Volume 175, pp. 5-17.

Chow, J. S., Lee, C. & Engel, A., 2015. The influence of extracellular Polysaccharides, growth rte, adn free cocoliths on the coagulation effiency of Emiliania huxleyi. *Marine Chemistry,* Volume 175, pp. 5-17.
Colomer, J., Peters, F. & Marrase, C., 2005. Experimental analysis of coagulation of particles under low-shear flow. *Water Research,* Volume 39, p. 2994–3000.
Doubell, M., Yamazaki, H., Li, H. & Kokubu, Y., 2009. An advanced laser-based fluorescence microstructure profiler (TurboMAP-L) for measuring bio-physical coupling in aquatic system. *Journal of Plankton Research,* Volume 31, pp. 1411-1452.
Flower, S. & Knauer, G., 1986. Role of large particles in the transport of elements and organic compounds through the oceanic water column. *Prog. Oceanogr. ,* Volume 16, pp. 141-156.
Flower, S. W. & Knauer, G. A., 1986. Role of large particle in trasnport of elements and organic compounds through the oceanic water column. *Progress in Oceanography,* 16(3), pp. 147-194.
Franks, P. J. & Jaffe, J. S., 2001. Microscale distributions of phytoplankton:initial results from a two-dimensional imaging fluorometer, OSST. *Marine Ecology Progress Series,* Volume 220, pp. 59-72.
Franks, P. J. & Jaffe, J. S., 2008. Microscale variability in the distributions of large fluorescent particles observed in situ with a planar laser imaging fluorometer. *Journal of Marine Systems,* 69(3-4), pp. 254-270.
Goldman, J. C., 1984. Conceptual Role for Microaggregates in Pelagic Waters. *Bulletin of Marine Science,* 35(15), pp. 462-476.
Gotschalk, C. & Alldredge, A., 1989. Enhanced primary production and nutrient regeneration within aggregated marine diatoms. *Marine Biology,* Volume 103, pp. 119-129.
Graham, G., Davies, E., Nimmo-Smith, A. & Bowers, D., 2012. Interpreting LISST-100X measurements of particles with complex shape using digital in-line holography. *Journal of Geophysical research ,* 117(C05034), pp. 1-20.
Graham, G. & Nimmo-Smith, A., 2010. The application of holography to the analysis of size and settling velocity of suspended cohesive sediments. *Limnology and Oceanography : Methods,* Volume 8, pp. 1-15.
Gregory, P., 1961. The Microbiology of the Atmosphere. *Interscience Publishers.*
Guidi, L. et al., 2009. Effects of pytoplankton community on production, size and export of large aggregates : A world-ocean analysis. *Limnology Oceanography,* 54(6), pp. 1951-1963.

Guidi, L. et al., 2009. Effects of phytoplankton community on production, size and export of large aggregates; A world - Ocean analysis. *Limnology and Oceanography*, 54(6), pp. 1951-1963.
Hanawa, K. & Mitsudera, H., 1987. Variation of water system distribution in the sanriku coastal area. *Journal of the Oceanographical Society of Japan*, Volume 42, pp. 435-446.
Jackson, G., 1995. Comparing observed changes in particle size spectra with those predicted using coagulation theory. *Deep-Sea Research* , 42(1), pp. 159-184.
Jackson, G. A., 1995. Comparing observed changes in particle size spctra with those predicted using coagulation theory. *Deep-Sea Research II*, 42(1), pp. 159-184.
Jackson, G. A. & Checkley Jr, D. M., 2011. Particle size distributions in the upper 100m water column and their implications for animal feeding in the plankton. *Deep-Sea Research I,* Volume 58, pp. 283-297.
Jackson, G. A., Logan, B. E., Alldredge, A. L. & Dam, H. G., 1995. Combining particle size spectra from a mesocom experiment measured using photographic and aperture impedance(Coulter and Elzone) techniques. *Deep-Sea Research II* , 42(1), pp. 139-157.
Jackson, G. et al., 1997. Particle size spectra between 1μm and 1cm at Montrey Bay determined using multiple instruments. *Deep-Sea Research 1,* 44(11), pp. 1739-1767.
Kantha, L. H. & Clayson, C. A., 2000. *Small scale provrddrd om Grophysical Fluid Flows.* s.l.:Academic Press.
Kindler, K., Khalili, A. & Stocker, R., 2010. Diffusion-limited retention of porous particles at density interfaces. *PNAS,* 107(51), pp. 22163-22168.
Kiorboe, T., 2001. Formation and fate of marine snow : small- scale processes with large-scale implications. *Scientia Marina* , 65(2), pp. 57-71.
Knauer, G., Hebel, D. & Cipriano, F., 1982. Marine snow: major site of primary production in coastal water. *Nature,* Volume 300, pp. 630-631.
Knauer, n.d. 1982.
Kostoglou, M., Dovas, S. & Karabelas, A., 1997. On the steady-state size distribution of dispersions in breakage processes. *Chemical Engineering Science*, 52(8), pp. 1285-1299.
Kranck, K. & Milligan, T., 1988. Macroflocs from diatoms : in-situ photography of particles in Bedford Basin. *Marine Ecology Progress Series*, Volume 44, pp. 183-189.

Laurenceau-Cornex, E. C. et al., 2015. Phytoplankton morphology controls on marine snow sinking velocity. *Marine Ecology Progress Series,* Volume 520, pp. 35-56.
Li, X.-y., Zhang, J.-j. & Lee, J., 2003. Modelling particle size distribution dynamics in marine waters. Volume 38, pp. 1305-1317.
Li, X.-y., Zhang, J.-j. & Lee, J. H., 2004. Modelling particle size distribution dynamics in marine waters. *Water Reseach,* Volume 38, pp. 1305-1317.
Logan, B. E. et al., 1995. Rapid formation and sedimentation of lrge aggregates is predictable from coagulation rates(half-lives) of transparent expolymer particles(TEP). *Deep-Sea Research II*, 42(1), pp. 203-214.
Loomis, N. C., 2011. *Computational Imaging and Automated Identification for Aqueous Environments,* s.l.: Massachusetts Institute of Technology and Woods Hole Oceanographic Institution.
Lueck, R. G., 2005. In: *Marine Turbulence- theories, observations and models.* s.l.:Cambridge University Press, pp. 89-100.
Massey, F. J. J., 1951. The Kolmogorov-Smirnov test for goodness of fit. *Journal of the American Statistical Association,* 46(253), pp. 68-78.
McCave, I., 1975. Vertical flux of particles in the ocean. Volume 22, pp. 491-502.
McCave, I., 1983. Particulate size spectra, behaviour and origin of nepheloid layers over the Nova Sotian Continental Rise. *Journal of Geophysical Research,* Volume 88, pp. 7647-7666.
McCave, I., 1984. Size spectra and aggregation of suspended particles in the deep ocean. Volume 31, pp. 329-352.
Nasmyth, P., 1970. *Oceanic turbulence,* Vancouver: University of British Columbia.
Oakey, N. & Elliot, J., 1982. Dissipation within the surface mixed layer. *Journal of Physical Oceanography,* 12(2), pp. 171-185.
Owen, R. & Zozulya, A., 2000. In-line digital holographic sensor for monitoring and characterizing marine particulates. *Optical Engineering* , 39(8), pp. 2187-2197.
Passow, U. & Alldredge, A. L., 1995. Aggregation of a diatom bloom in a mesocosm: the role of transparent expolymer particles(TEP). *Deep-sea Research II,* 42(1), pp. 99-109.
Petrik, C. M., Jackson, G. A. & Checkley Jr, D. M., 2013. Aggregates and their distributions determined from LOPC observations made using an autonomous profiling float. *Deep-Sea Research I,* Volume 74, pp. 64-81.
Podgorska, W., 2006. Modelling of high viscosity oil drop breakage process in intermittent turbulence. *Chemical Engineering Science,* Volume 61, pp. 2986-2993.

Puskaric, S., 2012. Ecology of gel-like marine snow event in the northern Adriatic Sea. *Acta Adriatica,* 53(3), pp. 375-387.
Renosh, P. et al., 2014. High frequncy variability of particle size distribution and its dependency on turbulence over the sea bottom during re-suspension processes. *Continental Shelf Research,* Volume 77, pp. 51-60.
Riebesell, U., 1991. Particle aggregation during diatom bloom 1 Physical aspects. *Marine Ecology Progress Series,* Volume 69, pp. 273-280.
Riley, J. et al., 2012. The relative contribution of fast and slow sinking particles to ocean carbon export. *Global Biogeochemical sycles* , Volume 26, p. GB1026.
Serra, T., Colomer, J. & Logan, B., 2008. Efficiency of different shear devices on flocculation. *Water Researches* , Volume 42, pp. 1113-1121.
Serra, T., Colomer, J. & Logan, B. E., 2008. Efficiency of different shear devices on flocculation. *Water Research,* Volume 42, pp. 1113-1121.
Shanks, A., 2002. The abundance, vertical flux, and still-water and apparent sinking rates of marine snow in a shallow coastal wter column.. *Continental Shelf Research,* Volume 22, pp. 2045-2064.
Shanks, A. L. & Trent, J. D., 1980. Marine snow: sinking rate and potential role in vertical flux. *Deep Sea Research Part A. Oceanographic Research Papers,* 27(2), pp. 137-143.
Stemmann, L. et al., 2008. Volume dirstibution for particles between 3.5 to 2000µm in the upper 200m region of the South Pacific Gyre. *Biogeosciences,* Volume 5, pp. 299-310.
Talapatra, S. et al., 2013. Characterization of biophysical interactions in the water column using in situ digial holography. *Marine Ecology Progress Series,* Volume 473, pp. 29-51.
Turner, J. T., 2015. Zooplankton fecal pellets, marine snow, phytodetritus and the ocean's biological pump. *Progress in Oceanography,* Volume 130, pp. 205-248.